Experimental Verification of the Role of Electron Pressure in Fast Magnetic Reconnection with a Guide Field

W. Fox,[1,*] F. Sciortino,[2,†] A. v. Stechow,[3] J. Jara-Almonte,[1] J. Yoo,[1] H. Ji,[1] and M. Yamada[1]
[1]Princeton Plasma Physics Laboratory, Princeton, New Jersey 08543, USA
[2]Blackett Laboratory, Imperial College, London SW7 2BW, United Kingdom
[3]Max-Planck-Institut für Plasmaphysik, 17491 Greifswald, Germany

(Received 22 August 2016; revised manuscript received 30 November 2016; published 21 March 2017)

We report detailed laboratory observations of the structure of a reconnection current sheet in a two-fluid plasma regime with a guide magnetic field. We observe and quantitatively analyze the quadrupolar electron pressure variation in the ion-diffusion region, as originally predicted by extended magnetohydrodynamics simulations. The projection of the electron pressure gradient parallel to the magnetic field contributes significantly to balancing the parallel electric field, and the resulting cross-field electron jets in the reconnection layer are diamagnetic in origin. These results demonstrate how parallel and perpendicular force balance are coupled in guide field reconnection and confirm basic theoretical models of the importance of electron pressure gradients for obtaining fast magnetic reconnection.

DOI: 10.1103/PhysRevLett.118.125002

Magnetic reconnection, the change of magnetic topology in the presence of plasma [1], enables explosive conversion of magnetic field energy to plasma kinetic energy in space and laboratory plasmas. The change in magnetic topology allows the rapid heat transport associated with sawtooth relaxation and self-organization processes in magnetic fusion devices [2,3]. In many reconnecting plasmas in space [4–6], solar [7], and laboratory [8–13] plasmas, reconnection proceeds in the presence of a finite guide field (GF) such that the magnetic field lines meet at an angle less than 180°. In toroidal magnetic fusion devices, during tokamak sawteeth [14,15] and relaxation events in reversed field pinches [2], the GF is typically significantly larger than the reconnecting components.

Reconnection in laboratory and astrophysical plasmas typically occurs much faster than can be explained by the Sweet-Parker model, where dissipation is due solely to classical plasma resistivity. Accordingly, a significant effort of simulations of GF reconnection (e.g., Refs. [16–22]) has been to understand mechanisms for fast reconnection. Compared to antiparallel reconnection [23–26], the presence of a GF significantly changes the dynamics of reconnection layers because the reconnection electric field and GF are coaligned, producing large parallel electric fields which must be sustained over the ion-diffusion layer [17,18,20]. A theoretical breakthrough documented the role of two-fluid mechanisms (the Hall term and electron pressure term in the generalized Ohm's law) for obtaining fast reconnection and large parallel electric fields in extended MHD simulations of the sawtooth relaxation at strong GF [16–18]. An explosive onset [16,17] and fast, resistivity-independent reconnection rates [18] were obtained in simulations which included the electron pressure gradient in the generalized Ohm's law, for current sheets thinner than the two-fluid scale $\rho_s = c_s/\omega_{ci}$ (where $c_s = \sqrt{T_e/m_i}$ is the ion-sound speed and $\omega_{ci} = eB/m_i$ is the ion gyrofrequency. These two-fluid simulations found that electron density and pressure variation with a quadrupolar pattern formed in the reconnection layer, and they showed that, even in 2D axisymmetric systems, the in-plane pressure gradient balanced a significant fraction of the parallel electric field and controlled the reconnection rate [16–18].

Previous experiments have reported some features consistent with this two-fluid GF reconnection model: Egedal *et al.* [10] showed that fast, spontaneous reconnection occurred coincident with the current sheet thinning to the ρ_s scale. Experiments have observed a progressive tilting of the plasma density [27] and the magnetic field [12] in the current sheet with a GF, which were attributed qualitatively to the $\mathbf{j} \times \mathbf{B}$ interaction of the Hall currents with the GF. However, none of these laboratory experiments directly observed the quadrupolar pressure variation or, more importantly, assessed its role in the generalized Ohm's law. Contemporaneous with the work here, the Magnetosphere Multiscale (MMS) mission reported a density variation during a current sheet crossing [28] consistent with a quadrupolar density variation. However, the single-pass data from a small number of spacecraft leaves ambiguity as to the global 2D (or 3D) structure of the reconnection layer, and again the importance of the electron pressure variation in the generalized Ohm's law was not assessed, though understanding the generalized Ohm's law remains a goal of the MMS mission [29,30].

In this Letter we report on the definitive observation and quantitative analysis of the predicted quadrupolar variation of the electron pressure along the reconnection separatrices during magnetic reconnection with a GF. Comprehensive 2D profile measurements of density,

temperature, and electric and magnetic fields obtained over ~1000 reproducible discharges allow a quantitative assessment of the role of these effects in the generalized Ohm's law for the parallel electric field [17,18] for the first time,

$$E_{||} = -\frac{\nabla_{||} p_e}{ne} - \frac{(\nabla \cdot \Pi_e)_{||}}{ne} + \frac{m_e dj_{||}/dt}{ne^2} + \eta j_{||}. \quad (1)$$

We show that the resulting parallel gradient of electron pressure, $\nabla_{||} p_e$, obtained from projecting the in-plane pressure gradient along the magnetic field, balances the parallel electric field $E_{||}$. Conversely, the 2D profile also allows measurement of the region where $E_{||}$ is *not* balanced by the pressure gradient, which defines the electron diffusion region (EDR), where the parallel electric field instead must be balanced by a combination of the anisotropic (e.g., Ref. [31]) or nongyrotropic pressure tensor $\nabla \cdot \Pi_e$ [19,21], electron inertia $dj_{||}/dt$, and other anomalous dissipation. The full width of the EDR is observed to be about $2\rho_s$ to $3\rho_s$ into the downstream away from the x point along the outflow direction. We also show experimentally that the electron pressure and guide magnetic field pressure variations are in force balance across the magnetic field. The Hall current inflows near the reconnection layer therefore have a significant diamagnetic component. The results are of particular interest for comparison with spacecraft observations by MMS; at present, there are only loose bounds on the diffusion region size from spacecraft measurements in the GF regime [30].

The present experiments were conducted on the Magnetic Reconnection Experiment (MRX, Fig. 1) [12,32]. The flux cores contain both poloidal field (PF) and toroidal field (TF) windings. The reconnecting, poloidal magnetic field is first established by current flowing in the PF coils, followed by plasma breakdown driven by induction through changing current in the TF windings. In these experiments, the TF windings are used in a null-helicity configuration [32], which applies little toroidal GF at the current sheet, and instead a $1/R$ toroidal field is applied by an axial GF winding. The plasma displays paramagnetism of the toroidal field on the global scale (~20 cm) due to a compressive motion of plasma and toroidal magnetic flux into the downstream flux core region [12]. Magnetic reconnection is driven by a combination of ramping down the PF current ("pull" reconnection [32]), and ramping up current in upstream "drive" coils [33].The newly installed drive coils increase the physical reconnection electric field and help to enter the current sheet reproducibly on the magnetic probe array.

MRX discharges are conducted using helium plasma at gas fill pressures of 4 mTorr, against base pressures of 2×10^{-6} Torr, obtaining $n_e = 1.5$–2.5×10^{19} m^{-3} and $T_e = 6$–8 eV in the current sheet. The flux core separation was 40 cm from surface to surface. Typical reconnection electric fields of order 120–150 V/m are obtained. These

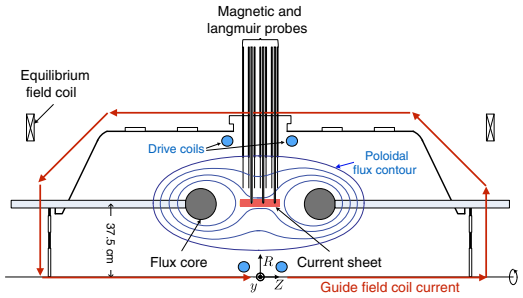

FIG. 1. Schematic of the MRX device, showing the location of flux cores, upstream drive coils, and probe arrays. The coordinate system uses the right-hand triplet (Z, R, y).

electric fields, normalized to upstream Alfvenic rates $B_{\rm rec} V_{A,\rm rec}$, are 0.2–0.3, evaluated using the reconnecting components of the field 4 cm upstream of the x point. The ion-sound gyroradius is roughly 4 cm using the total upstream magnetic field $|B| = (B_{\rm rec}^2 + B_g^2)^{1/2} \approx 15$ mT. As our analysis focuses on quantifying 2D, axisymmetric reconnection mechanisms, we use a lower-current-density regime of MRX which does not display highly transient, 3D flux-rope structures in the current sheet [33].

Detailed plasma profiles covering the "in-plane" coordinates (R, Z) are reconstructed from magnetic probes and scanned Langmuir probes (Fig. 2). MRX employs hundreds of three-axis magnetic pickup coils, enabling a full 2D map of the magnetic fields each discharge. Plasma density, temperature, and in-plane electric fields are measured by one to three Langmuir probes; 2D profiles are assembled from a large set of discharges. In assembling the data set, we correct for shot-to-shot variation in the x-line position using the relative position of the probes from the measured x point. Additionally, fixed-position reference Langmuir probes and the global magnetic measurements are used to discriminate which scanned probe data to include in the final data set. To map the point data to a grid, we use a radially weighted averaging with a Gaussian weighting function with a smoothing radius of 1.5 cm. To account for errors and uncertainty in this technique, including shot-to-shot variation in probe signals and x-point location, we use a statistical bootstrapping method in which quantities are recalculated over a large number of random subsets of the data. This yields a set of realizations of the processed data, from which means and confidence intervals are calculated [34].

Figure 2 shows a detailed comparison of plasma profiles obtained from two experimental campaigns carried out at opposite signs of GF. At positive GF [Figs. 2(a)–2(c)], $B_g = +0.8 B_{\rm up}$, three Langmuir probes were simultaneously scanned and the profile is constructed from 280 discharges. At negative GF [Figs. 2(d)–2(f)], $B_g = -0.75 B_{\rm up}$, a single probe was scanned over 850 discharges. Axis positions (ΔZ, ΔR) on the figure are given with respect to the reconnection x point. Figures 2(a) and 2(d) show the plasma current density, which is observed to tilt and extend along the high-density separatrix.

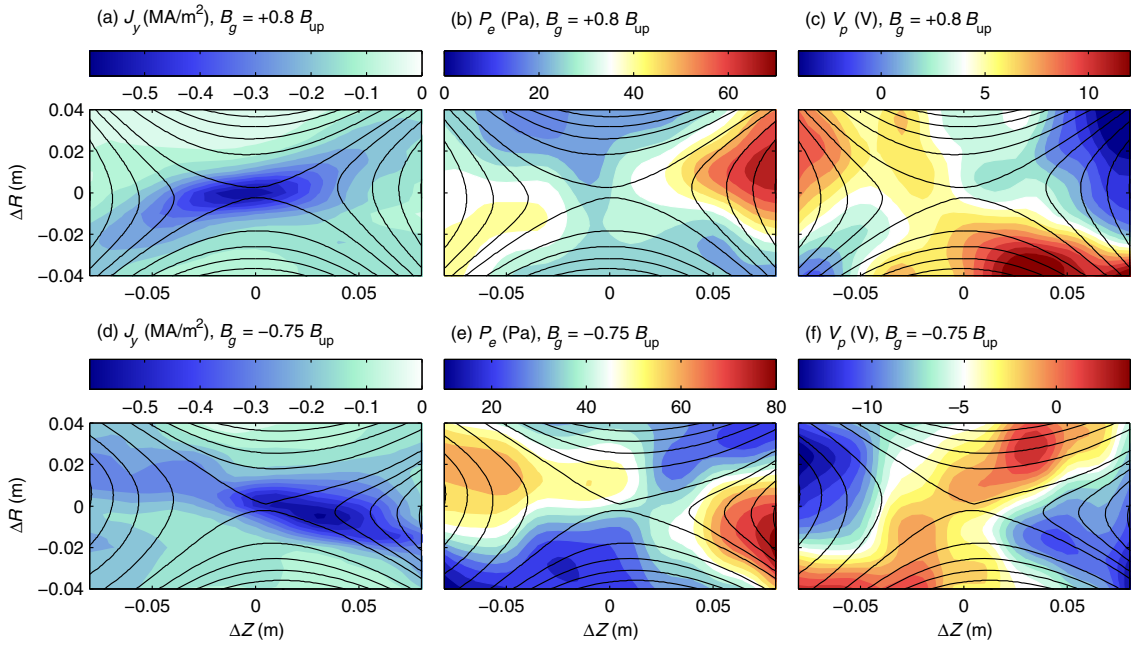

FIG. 2. Comparison of plasma profiles at (a–c) positive and (d–f) negative GFs. (a),(d) Plasma current density. (b),(e) Electron pressure. (c),(f) Plasma potential.

The electron pressure, shown in Figs. 2(b) and 2(e), is observed to have a significant quadrupolar pattern. The sign of the electron pressure variation flips with the applied GF, which is consistent with the associated $\nabla_{||} p_e$ balancing $E_{||}$. Furthermore, the pressure variations are not a result of a symmetric pressure profile tilting along with the magnetic field profile; instead, the pressure differences are maintained *along* field lines from one separatrix to another. The magnitude of these pressure variations is quite large: for a positive GF, electron pressures vary from 50 Pa $(\Delta Z, \Delta R) = (+0.07\text{ m}, +0.035\text{ m})$ to 25 Pa $(+0.07, -0.035)$, a factor of 2. Similarly, at negative GFs, we measure an opposite but similarly large pressure variation from 60 Pa $(+0.07, -0.03)$ to 20 Pa $(+0.07, +0.03$, a factor of 3. Therefore, we quantitively establish very large quadrupolar pressure variations (100% or larger) between separatrices in GF reconnection. Beyond the data shown here, quadrupolar pressure profiles were also obtained in previous data sets in both He and D_2 plasma.

The plasma potential V_p, shown in Figs. 2(c)–2(f), is also observed to have a predominantly quadrupolar pattern, as has been measured in previous GF reconnection experiments at the VTF [9,10]. Such a structure is required to obtain $E_{||} = 0$ on MHD scales and is also consistent with $\mathbf{E} \times \mathbf{B}$ plasma flows through the current sheet. V_p is measured from Langmuir probes using $V_p = V_f + 3.6T_e$ [35], where V_f is the floating potential and T_e the measured electron temperature.

The large quadrupolar plasma pressure and in-plane potential variations are qualitatively consistent with the two-fluid reconnection picture in the presence of a GF. We now quantitatively analyze two aspects of this, first the in-plane force balance between field and pressure, and second the contribution of the electron pressure gradient to the parallel Ohm's law.

First, the electron pressure variation is consistent with the $\mathbf{j} \times \mathbf{B}$ force between the in-plane Hall current and the GF and is analyzed in Fig. 3. Figure 3(a) shows the overall structure of the reconnecting field across the current sheet, taken along a cut at $\Delta Z = 0$. Figure 3(b) shows cuts of the out-of-plane B_y component of the field at $\Delta Z = -0.04$, 0, and $+0.04$ m (the error band indicates the 90% confidence interval). The differences between -0.04 and 0.04 m are due to the quadrupolar pattern of enhancement and the depletion of the GF [12]. Figure 3(c) then displays quantitative cuts of the plasma pressure and magnetic field pressure variations. We measure pressure differences at a constant radius ΔR, between $\Delta Z = -0.04$ m and $\Delta Z = +0.04$ m, approximately $1\rho_s$ on each side of the x point. The red band shows the GF pressure variation (90% confidence interval), $\Delta B_y^2/2\mu_0$, which is quantitatively evaluated as $\int j_R B_y dZ$ from the magnetic field data. (A secondary magnetic force term $\int j_y B_R dZ$ is small, both because B_R is small in the inflow regions and because of the symmetry of the integration limits with respect to the x point—and therefore not shown.) The blue bands show the electron pressure difference (68% and 90% confidence intervals). The GF pressure variation is complementary to the electron pressure variation, consistent with force balance, and the pressure difference peaks approximately $0.5\rho_s$ upstream of the x points. At $\Delta R = +0.02$ m, from left to right, the electron pressure

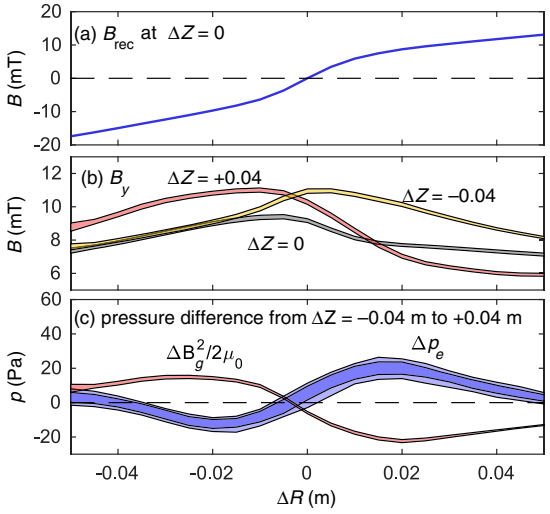

FIG. 3. Radial profiles. (a) The reconnecting component of a magnetic field at $\Delta Z = 0$. (b) Out-of-plane field B_y at $\Delta Z = -0.04$ (red), 0 (gray), and $+0.04$ m (yellow). (c) Electron pressure (blue) and GF pressure (red) differences between $\Delta Z = -0.04$ and $+0.04$ m. Measurements are at positive GF ($B_g = +0.8B_{\rm up}$).

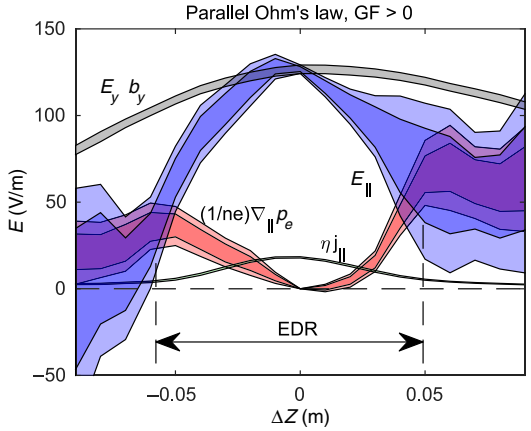

FIG. 4. Parallel components of Ohm's law evaluated along a cut along the outflow direction of the current sheet, along $\Delta r = 0$. (Gray) Inductive component of the E field $E_y b_y$. (Blue) Full $E_\parallel = \mathbf{E}\cdot\mathbf{b} = E_y b_y - \nabla_r\Phi\cdot b_r$. (Red) Parallel gradient of electron pressure $(1/ne)\nabla_\parallel p_e$. (Green) Classical resistivity $\eta_{Sp} j_\parallel$. The EDR, where $E_\parallel$ is not balanced by $\nabla_\parallel p_e$, significantly beyond error bars, is observed to extend from -0.06 to $+0.05$ m.

increases by 18 ± 5 Pa (90% confidence), while the magnetic pressure decreases by 22 ± 1 Pa. At $\Delta R = -0.02$ m, the electron pressure decreases by 12 ± 4 Pa, while the magnetic pressure increases by 15 ± 1 Pa. These are in balance with each other, within error bars; however, due to the relatively large error bars, additional ion pressure variations (not measured), cannot be excluded.

We now demonstrate that the pressure variation is also coupled to the parallel force balance. Figure 4 shows the evaluation of relevant terms of the parallel Ohm's law along the outflow direction at $\Delta R = 0$. The total parallel electric field $E_\parallel$ (in blue, bands indicate 68% and 90% confidence intervals) has both an out-of-plane, inductive component and an in-plane, dominantly electrostatic component. The inductive component, $E_y b_y$, where $\mathbf{b} = \mathbf{B}/|B|$, shown in gray, is evaluated from the magnetic probe measurements and is finite throughout the downstream. The net parallel electric field $E_\parallel$, however, has an additional structure due to the in-plane E_r which is evaluated from the plasma potential (Fig. 2). For this cut at $\Delta R = 0$, $b_z = 0$ and $E_\parallel = E_y b_y + E_r b_r$. At the x point, the in-plane component vanishes. As one progresses into the downstream, near $\Delta Z = +0.05$ m, the in-plane component *partly* balances the out-of-plane component; however, 50 ± 25 V/m remains uncompensated. Here, we observe that the electron pressure gradient term, $\nabla_\parallel p_e = b_r \partial_r p_e$, contributes an additional 60 ± 25 V/m to balance the Ohm's law through the rest of the measured downstream (red bands indicate 68% and 90% confidence intervals).

Returning to near the x point ($\Delta Z = 0$), we find that $E_\parallel$ is unbalanced, even accounting for $\nabla_\parallel p_e$. In this region, the classical Spitzer resistivity is also too low (by about a factor of 8) to balance the parallel electric field. This region defines the EDR where a combination of collisionless effects including electron inertia, the pressure tensor, and other anomalous resistivity must play a role to balance the electric field. Experimentally, we observe this region of unbalanced $E_\parallel$ extends to a full width of 8–12 cm ($2\rho_s$ to $3\rho_s$) along the outflow direction. We also measure an EDR width of the order 1–3 cm in the narrower inflow direction, comparable to the current sheet width. However, this is challenging to resolve below the 1 cm probe resolution in the scan, and a definitive measurement including scaling with various parameters of the current sheet will await future work, where we will explore all of these dissipation mechanisms in greater detail. For the time being, we note that an available theory [21] for the magnitude of the pressure tensor for GF reconnection requires a diffusion region width on the order of the electron gyroscale ρ_e for a significant pressure tensor contribution. In the present experiments, $\rho_e \approx 1$ mm, which is significantly narrower than the observed EDR. This suggests that the electron pressure tensor may not be a significant effect during GF reconnection in the MRX, consistent with previous findings at zero GF [36]. Preliminary measurements of pressure anisotropy of $\lesssim 20\%$ in the MRX suggest that this effect also does not balance the parallel electric field; the small anisotropy is consistent with the finite collisionality of the MRX, where the electron collision frequency is significantly faster than times for the electron fluid to cross the reconnection layer, as has recently been analyzed in a collisional particle-in-cell simulation [37]. Further candidate mechanisms to obtain momentum balance include anomalous resistivity or viscosity due to wave-particle interactions [11,38,39].

To conclude, we have presented detailed plasma and field profiles in a reconnection layer with a GF,

demonstrating the existence of the long-predicted quadrupolar electron pressure structure, the pressure balance between it and the GF pressure, and its role in the generalized Ohm's law. By documenting parallel electric fields and quadrupolar pressure variations, this physics can become a tool to understand fast magnetic reconnection with a GF in other space and laboratory plasmas [28,29]. The scaling of the EDR with GF strength and collisionality, and the mechanisms to balance the electric field in the electron diffusion region will be explored in future work.

The digital data for this paper can be found at [40].

This work was supported by the Max-Planck Princeton Center for Plasma Physics, funded by the U.S. Department of Energy under Contract No. DE-AC0204CH11466 and NASA under Agreements No. NNH15AB29I and No. NNH14AX631. F. S. acknowledges support from the European Fusion Education Network under the EUROfusion Consortium and the European Union's Horizon 2020 research and innovation program under Grant Agreement No. 633053. The authors thank Professor A. Bhattacharjee for valuable discussions.

*wfox@pppl.gov
†Present address: Department of Physics, Massachusetts Institute of Technology, Cambridge, Massachusetts 02139, USA.

[1] M. Yamada, R. Kulsrud, and H. Ji, Rev. Mod. Phys. **82**, 603 (2010).
[2] J. B. Taylor, Rev. Mod. Phys. **58**, 741 (1986).
[3] R. J. Hastie, Astrophys. Space Sci. **256**, 177 (1997).
[4] M. Øieroset, R. P. Lin, T. D. Phan, D. E. Larson, and S. D. Bale, Phys. Rev. Lett. **89**, 195001 (2002).
[5] T. D. Phan, J. T. Gosling, G. Paschmann, C. Pasma, J. F. Drake, M. Øieroset, D. Larson, R. P. Lin, and M. S. Davis, Astrophys. J. **719**, L199 (2010).
[6] J. P. Eastwood, M. A. Shay, T. D. Phan, and M. Øieroset, Phys. Rev. Lett. **104**, 205001 (2010).
[7] S. Masuda, T. Kosugi, H. Hara, S. Tsuneta, and Y. Ogawara, Nature (London) **371**, 495 (1994).
[8] W. Gekelman and R. L. Stenzel, J. Geophys. Res. **86**, 659 (1981).
[9] J. Egedal, A. Fasoli, and J. Nazemi, Phys. Rev. Lett. **90**, 135003 (2003).
[10] J. Egedal, W. Fox, N. Katz, M. Porkolab, K. Reim, and E. Zhang, Phys. Rev. Lett. **98**, 015003 (2007).
[11] W. Fox, M. Porkolab, J. Egedal, N. Katz, and A. Le, Phys. Rev. Lett. **101**, 255003 (2008).
[12] T. D. Tharp, M. Yamada, H. Ji, E. Lawrence, S. Dorfman, C. E. Myers, and J. Yoo, Phys. Rev. Lett. **109**, 165002 (2012).
[13] H. Tanabe *et al.*, Phys. Rev. Lett. **115**, 215004 (2015).
[14] S. von Goeler, W. Stodiek, and N. Sauthoff, Phys. Rev. Lett. **33**, 1201 (1974).
[15] M. Yamada, F. M. Levinton, N. Pomphrey, R. Budny, J. Manickam, and Y. Nagayama, Phys. Plasmas **1**, 3269 (1994).
[16] A. Y. Aydemir, Phys. Fluids B **4**, 3469 (1992).
[17] X. Wang and A. Bhattacharjee, Phys. Rev. Lett. **70**, 1627 (1993).
[18] R. G. Kleva, J. F. Drake, and F. L. Waelbroeck, Phys. Plasmas **2**, 23 (1995).
[19] P. Ricci, J. U. Brackbill, W. Daughton, and G. Lapenta, Phys. Plasmas **11**, 4102 (2004).
[20] M. Swisdak, J. F. Drake, M. A. Shay, and J. G. McIlhargey, J. Geophys. Res. **110**, A05210 (2005).
[21] M. Hesse, Phys. Plasmas **13**, 122107 (2006).
[22] P. A. Cassak, J. F. Drake, and M. A. Shay, Phys. Plasmas **14**, 054502 (2007).
[23] X. Wang, A. Bhattacharjee, and Z. W. Ma, J. Geophys. Res. **105**, 27633 (2000).
[24] J. Birn *et al.*, J. Geophys. Res. **106**, 3715 (2001).
[25] F. S. Mozer, S. D. Bale, and T. D. Phan, Phys. Rev. Lett. **89**, 015002 (2002).
[26] Y. Ren, M. Yamada, S. Gerhardt, H. Ji, R. Kulsrud, and A. Kuritsyn, Phys. Rev. Lett. **95**, 055003 (2005).
[27] A. G. Frank, S.Yu. Bogdanov, G. V. Dreiden, V. S. Markov, and G. V. Ostrovskaya, Phys. Lett. A **348**, 318 (2006).
[28] M. Øieroset *et al.*, Geophys. Res. Lett. **43**, 5536 (2016).
[29] R. E. Ergun *et al.*, Phys. Rev. Lett. **116**, 235102 (2016).
[30] S. Eriksson *et al.*, Phys. Rev. Lett. **117**, 015001 (2016).
[31] A. Le, J. Egedal, O. Ohia, W. Daughton, H. Karimabadi, and V. S. Lukin, Phys. Rev. Lett. **110**, 135004 (2013).
[32] M. Yamada, H. Ji, S. Hsu, T. Carter, R. Kulsrud, N. Bretz, F. Jobes, Y. Ono, and F. Perkins, Phys. Plasmas **4**, 1936 (1997).
[33] J. Jara-Almonte, H. Ji, M. Yamada, J. Yoo, and W. Fox, Phys. Rev. Lett. **117**, 095001 (2016).
[34] B. Efron, *The Jackknife, the Bootstrap and Other Resampling Plans* (Society for Industrial and Applied Mathematics, Philadelphia, 1982).
[35] J. Yoo, M. Yamada, H. Ji, and C. E. Myers, Phys. Rev. Lett. **110**, 215007 (2013).
[36] H. Ji, Y. Ren, M. Yamada, S. Dorfman, W. Daughton, and S. P. Gerhardt, Geophys. Res. Lett. **35**, L13106 (2008).
[37] A. Le, J. Egedal, W. Daughton, V. Roytershteyn, H. Karimabadi, and C. Forest, J. Plasma Phys. **81**, 30581 0108 (2015).
[38] W. Fox, M. Porkolab, J. Egedal, N. Katz, and A. Le, Phys. Plasmas **17**, 072303 (2010).
[39] A. von Stechow, O. Grulke, and T. Klinger, Plasma Phys. Controlled Fusion **58**, 014016 (2016).
[40] http://arks.princeton.edu/ark:/88435/dsp01x920g025r.